

CFD SIMULATION OF THE VATTENFALL 1/5TH-SCALE PWR MODEL FOR BORON DILUTION STUDIES

T. V. Dury¹, B. Hemström² and S. V. Shepel¹

¹Paul Scherrer Institute (PSI), 5232 Villigen PSI, Switzerland

²Vattenfall Utveckling AB, Älvkarleby, Sweden

Abstract

The VATT-02 experiment, performed at Vattenfall, Sweden, with a 1/5th-scale model of a 3-loop PWR pressure vessel, has been simulated with the Computational Fluid Dynamics (CFD) code CFX-5 at PSI, Switzerland. The simulations were initially part of the FLOMIX-R EU 5th Framework Programme, aimed at providing validation data prior to CFD codes being used to model full-size nuclear vessels. These studies were extended at PSI to examine mesh effects. Steady-state velocities and transient boron concentration distributions were plotted, and their sensitivity to different CFD models and mesh refinement examined. Steady-state velocities in the downcomer were not in good agreement with experiment at all instrumentation locations, but, nevertheless, predicted transient boron distribution and its minimum concentration at the core inlet were close to the measured data. Useful conclusions could be drawn for application to full reactor size.

Introduction

There exists a potential risk of a reactivity accident occurring in a Pressurised Water Reactor (PWR) if a slug of water with a low concentration of boron (as reactivity inhibitor) passes into the vessel and core under certain conditions of Reactor Cooling Pump (RCP) start-up. This could happen by accident if the reactor is at decay heat level and natural circulation has been stopped. It is therefore essential to determine if a substantial reactivity change could occur. This would be carried out by using neutronics codes after the distribution of the degree of boration of the fluid within the core is known.

The present CFD study began as a contribution to the FLOMIX-R Project of the 5th EURATOM Framework Programme [1], initiated as a follow-up to the 4th Framework EUBORA Concerted Action [2]. The Computational Fluid Dynamics (CFD) codes FLUENT [3] and CFX-5 [4] were used to simulate the VATT-02 experiment performed in the test facility at Vattenfall Utveckling AB, Älvkarleby, Sweden — a 1/5th-scale model of the pressure vessel and internal components of a 3-loop Westinghouse PWR, with pump flow-rate behaviour applied corresponding to RCP start-up under various non-design operating conditions. This report refers only to the results obtained with CFX-5, as these were closer to the measured data for both steady-state and (particularly) for transients.

The object of the CFD study was to: a) simulate steady-state conditions with constant flow in one cold leg and the pumps in the other two legs stopped; b) compare predicted and measured velocity distributions within the downcomer at given vertical planes; and c) simulate a transient experiment in which the equivalent of a plug of water with a lower boron concentration was injected through this single cold leg at a known rate and with a known total volume.

Experiment

CFD calculations were performed by PSI for the VATT-02 test from the Vattenfall series of four experiments, VATT-01 to VATT-04. All tests were slug mixing transients, representing a slug of low boron concentration initially present in one of the Reactor Coolant System (RCS) pipes. A photograph of the central section of the model facility is shown in Fig. 1, with a schematic of the full facility layout given in Fig. 2 and a vertical cross-section of the model reactor vessel in Fig. 3. All dimensions given in Fig. 3 are in millimetres, and are for the model facility, not for the plant.



Fig. 1: Vattenfall 1/5th-scale PWR model facility

All external model components were constructed of Plexiglas®, to allow flow measurement and visualisation to be made. As the core was not modelled, or flow within it examined, the core outlet was modified in the facility to allow fluid to exit vertically instead of via the hot-leg penetrations in the vessel wall. Internal model components were either constructed of Plexiglas® or steel, and instrumentation in the lower vessel plenum was incorporated within support columns connecting the different horizontal support plates in the region from the base of the dome up to the Core Inlet Plate.

The model used tap water to simulate the borated water originally within the system, heated to 53.6°C to maximise the Reynolds number [5]. The supply tank for the tap water had a volume of 15 m³, in the form of a horizontal cylinder with a length of 6m and diameter of 1.8 m. The water level within it was kept at approximately 200mm below the roof of the tank and was relatively stable during transient experiments. Heat-loss effects on slug volume and mixing are recognised, but have been impossible to quantify. They are, however, thought to be relatively small.

Water with relatively low boron content (for the slug) was represented by a salt-water solution, with a suitable amount of an organic fluid added, with a lower density than water, to bring the average mixture density so close to that of the tap water that buoyancy forces were negligible. This slug fluid will from now on be referred to as ‘de-borated water’ and the tap water as ‘borated’ water. The local concentration of de-borated fluid was measured above the Core Support Plate (Fig. 3) by means of a grid of conductivity probes.

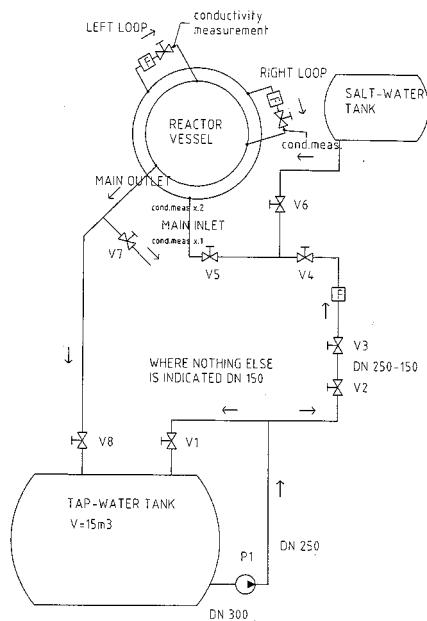


Fig. 2: Schematic of the facility

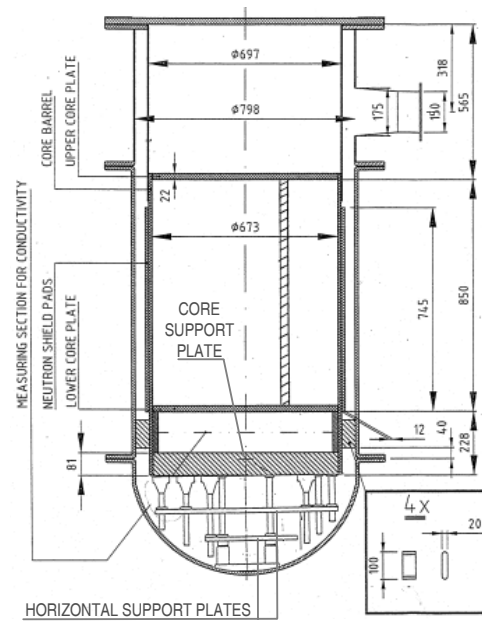


Fig. 3: Vertical cross-section of the vessel

The layout of the cold-leg pipes can be seen in the views of the CAD model in Fig. 4, and in a view from below in Fig. 5. In the global coordinate system indicated in these Figures, the vertical coordinate, Z, was defined to be zero at the level of the centre of the main inlet pipe (the RCS pipe), and is directed upwards. Both X and Y coordinates are zero at the core axis, with X aligned with the axis of the section of the RCS pipe joining the downcomer. Positive angles are to the right of this position and negative angles to the left, viewed from above (Fig. 4). The cold legs carrying low flow out of the model are defined as the left and right loops.

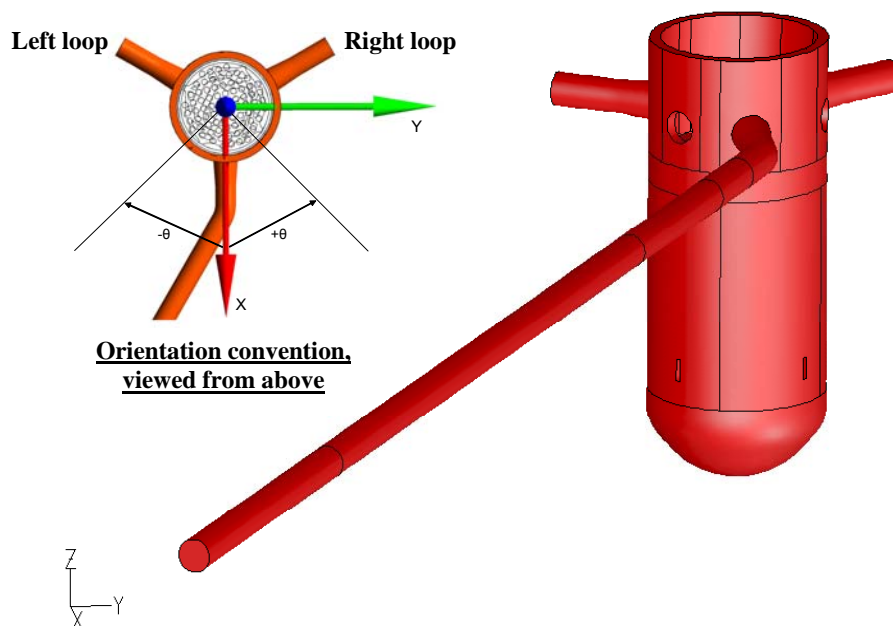


Fig. 4: Perspective view of the CFD model, and orientation convention

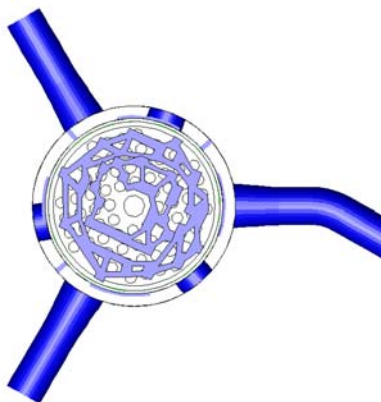


Fig. 5: View of CAD model from below, showing the two cut-away horizontal support plates, inlet pipes, and penetrations

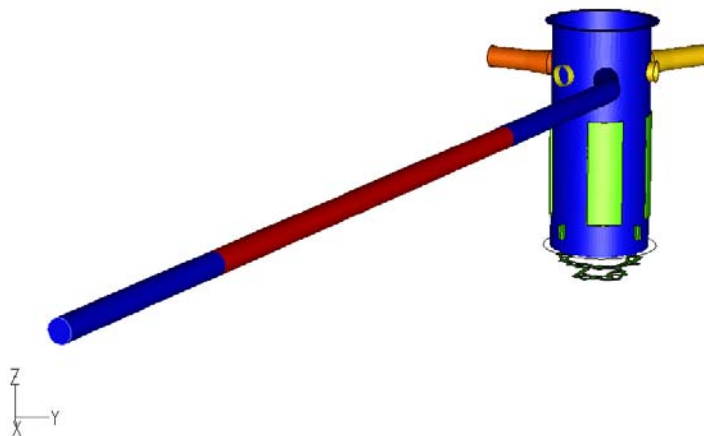


Fig. 6: Perspective view of vessel showing 3 or the 4 thermal shields and the support blocks in the downcomer (light green), inlet pipes (light brown) and fluid slug (dark brown)

The Reynolds number was one-tenth of that in the real power plant; for example, 78000 in the downcomer at the transient time when the de-borated slug reached the measuring plane below the core inlet. The transient ramp length was adjusted so that the Strouhal number (the ratio of forces due to transient and convective accelerations) was the same in the test vessel as in the plant. Dimensionless concentrations for mixtures of the two solutions were obtained by means of 181 probes located 70 mm below the Lower Core Plate, at $Z = -1.129$ m (Fig. 3). Vertical and tangential/circumferential velocities in the downcomer were measured using Laser Doppler Velocimetry.

CFD modelling

The CFX-5.6 version of the code was used for most steady-state simulations, and the later version, CFX-5.7, was used for all transients. The advantage of the latter version lay solely in its greater selection of turbulence models, and improvements to some existing models. However, none of these changes influenced the conclusions drawn from calculations already performed with CFX-5.6.

After a study of mesh effects made at Vattenfall, Grids 1 and 2 (the latter being a $\frac{1}{2} \times \frac{1}{2} \times \frac{1}{2}$ subdivision of Grid 1) were created using the FLUENT pre-processor Gambit, applying the Best Practice Guidelines for CFD [6]. Hexahedral cells were used for the inlet pipe, the downcomer and the upper $\frac{5}{6}$ th of the core, to obtain the greatest accuracy of solution, while tetrahedral cells were used, for convenience, in the lower plenum, the holes in the Core Support Plate, the volume between the Core Support Plate and the Core Inlet Plane, and the lower $\frac{1}{6}$ th of the core. A layer of prisms was applied at the lower plenum wall, and pyramid cells as the transition between hexahedral and tetrahedral cells.

Four new grid models were created after FLOMIX-R had ended (Grids A to D, with differences detailed in Table 2), to try to reduce the number of grid cells while not degrading the computational accuracy of solution. The numbers and types of cells of all grids are summarised in Table 1. Some internal structures were omitted in all grids, such as the vertical support rods and lowest supporting plate in the lower plenum, and small structures and protrusions in the downcomer. Some internal structures were simplified, e.g. not modelling the chamfers on the thermal shields (Grids 1 and 2), or the lower plenum supporting plate thicknesses. Calculation with Grid 1 without any supporting plates in the lower plenum had showed that their omission significantly de-stabilised the flow, and so they were retained for all simulations referred to here.

Table 1: Cells and their types for all grids

Grid	Number and type of cells				
	Inlet pipe	Downcomer	Lower Plenum (to core)	Core	Total
1	20224 (H [†])	106695 (H)	61781 (T [†] + layer of Pr [†] at wall)	12026 (H for upper 5/6 and T for lower 1/6)	200726
2	161792 (H)	853560 (H)	494248 (T + layer of Pr at wall)	96208 (H for upper 5/6 and T for lower 1/6)	1605808
A	63000 (H, incl. part of lower plenum)		324000 (T + 20000 Py [†])	27999 (Pr)	434000
B	63000 (H, incl. part of lower plenum)		324000 (T + 20000 Py)	27999 (Pr)	434000
C	63000 (H, incl. part of lower plenum)		324000 (T + 20000 Py)	27999 (Pr)	434000
D	58000 (H, incl. part of lower plenum)		324000 (T + 20000 Py)	27999 (Pr)	429000

[†] H= Hexagonal; T=Tetrahedral; Pr=Prism; Py=Pyramid

For all grids, the core was modelled as a porous volume with an inertial momentum sink. The resistance coefficients per unit length, based on the superficial velocity, were set to 2.28 m^{-1} for the vertical direction and 95.9 m^{-1} for the horizontal direction, estimated from the VDI-Wärmeatlas [7], with a volume porosity of 0.559. The core inlet and outlet plates had both been modelled with FLUENT as surfaces with inertial momentum sinks, with inertial resistance coefficient estimated from the handbook of Idelchik [8] to be 12.3, based on the superficial velocity. However, as CFX-5 could not represent momentum sinks at surfaces, these surface sinks were combined with, and distributed over, the sink over the full length of the core. After sensitivity studies with FLUENT, the CFD model exit plane was set at the core outlet.

Steel walls were modelled with a roughness height of 0.15 mm (thus modifying the wall function), but the Plexiglas® walls with zero roughness. The blocks centring the core barrel within the vessel were included in all grids except B. Vertical holes in the Core Support Plate were modelled explicitly.

In Grids 1 and 2, the two cut-away horizontal support plates in the lower plenum (Fig.5) were modelled as simple two-dimensional surfaces, i.e. with no vertical thickness, and located vertically at the upper plate surfaces, but only minor simplifications were made from the outlines of the actual manufactured parts. However, the four grids A, B, C and D differed in the way that the support plates, centring blocks and inlet pipe were treated, as described in Table 2. For Grids A to D, the inlet pipe, downcomer and part of the lower plenum were modelled with hexahedral cells, the rest of the lower plenum was meshed with tetrahedral cells, and the core meshed with prisms. Pyramids connected hexahedral and tetrahedral cells.

Table 2: Details of Grids A, B, C and D

GRID	Thickness of both lower plenum supporting plates (mm)	Centring blocks	Inlet pipe
A	17	included	long, bent
B	17	not included	long, bent
C	0	included	long, bent
D	17	included	short, straight

A simplification made for Grids A, C and D was that a slip boundary condition was set for the centring blocks, as their dimensions were smaller than those of the grids in this region and thus the code could not in any case resolve the velocity profile over them.

During the transient, Fortran functions representing measured inlet and loop outlet flow-rates were used instead of by interpolation from the actual measured data. As all flow-rates were zero up to 1.5 s, transient calculations were started at $t = 1.5$ s. Radial and tangential velocities were set to zero. The inlet turbulence intensity and the hydraulic diameter were set to 10% and 5 mm, respectively. Putting the inlet boundary far upstream of the downcomer reduced the need for sensitivity tests, and therefore no tests on its position or the boundary conditions were made. The two loop outlets were positioned approximately three diameters downstream of the downcomer, and the flow-rate functions applied across the outlet planes. No sensitivity tests were made for the position and condition for these outlets, as they were believed not to be important for the flow field in the downcomer. The mass flow-rates applied by the functions are plotted in Fig. 7 (note that the mass flow-rates in the left and right loops are negative, i.e. the flows are out of the vessel).

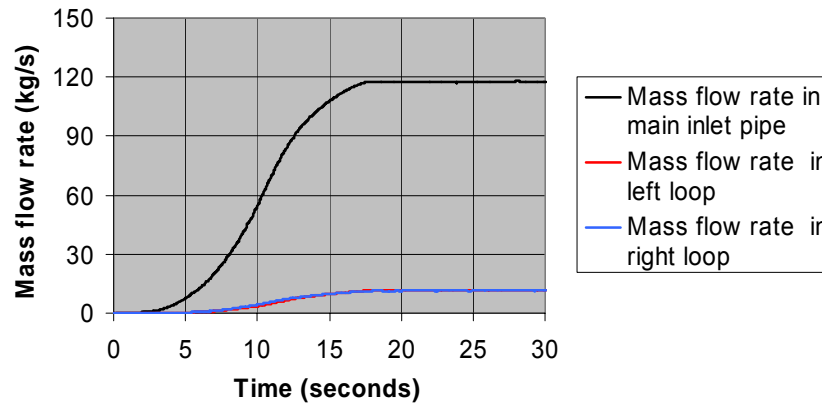


Fig. 7: Absolute mass flow-rates applied at the inlet pipe and the left and right outlet loops

Simulations were made using the following turbulence models: Standard $k-\epsilon$, RNG (Renormalised Group) $k-\epsilon$, Standard $k-\omega$ and Shear-Stress Transport (SST) $k-\omega$ models, and a number of different versions of the Reynolds Stress Model (RSM). The complete range of sensitivity tests was only made for steady-state conditions and for the coarse grid. For transient calculations, the RNG, SST and one of the RSM models in the code were used, with both coarse and fine meshes.

The default Incomplete Lower-Upper (ILU) factorisation technique applied to the Additive-Correction Algebraic Multi-Grid method was used throughout, as was the improved Rhie-Chow scheme for pressure/velocity coupling. The 1st-order Upwind and the High Resolution schemes for advection were applied and results compared. The latter scheme blends 1st-order and 2nd-order resolution according to the local gradient of the variable defined, and avoids numerical difficulties which can occur with a purely 2nd-order scheme (see [4] for details of the options).

For the k and ϵ terms in the appropriate turbulence equations, the 1st-order scheme was default and not intended to be changed, as it could be unstable. The High-Resolution scheme was, however, applied for these terms for some calculations, but with no obvious benefit. During the fine-mesh transient calculation (Grid 2) with the RNG model, the High Resolution scheme caused numerical instability between 4 s and 6 s and was replaced by the 1st-order Upwind on all variables. The calculation subsequently ran successfully from 6 s to 25 with the High Resolution scheme. The High Resolution scheme caused no such instability with the other two turbulence models when used with Grid 2.

constant time-step of 0.01667 s was used for all transients, corresponding to the sampling frequency of the experimental data collection. This time-step gave a maximum Courant number of around 30 with Grid 1. The only time-step sensitivity study was made with Grid A (see below). The 2nd-order Backward Euler scheme was always used for time, with the solution for each time-step initialised from the end of the previous one.

Convergence was smoother and lower ultimate residuals were achieved with 1st-order upwind advection, due to the influence of numerical diffusion, compared with the High Resolution scheme, which tended to give stable velocities but fluctuating RMS residuals. To check if fluctuating residuals were caused by instability of the flow field, a transient calculation of steady-state conditions was made with the RNG model and the coarse mesh. With a time-step of 0.01 s (less than the default value of 0.042 s set by the code), and for almost 700 time-steps, the calculated velocities and residuals still fluctuated. A normalised RMS residual limit of 10^{-6} for iterations within each time-step was set for momentum, pressure and turbulence quantities for all transients, as this was estimated from the steady-state calculations to be a sufficiently low value to ensure adequate convergence. As this limit could always be achieved with single-precision arithmetic, double-precision was never used (though it had to be used with FLUENT to reach this convergence level with transients).

Initial boron concentrations were set in the volume containing the slug of de-borated water (concentration = 0.0) and in the remainder of the facility (concentration = 1.0). The calculation was isothermal, with a water temperature of 53.6°C, density of 986.42 kg/m³ and dynamic viscosity of 5.156×10^{-4} Ns/m².

Steady-state results: Grids 1 and 2

Comparisons were made for vertical velocity, tangential velocity and velocity angle (flow direction) at two levels in the downcomer, one level at the middle height of the downcomer and one level closer to the bottom. Measurement positions are shown in Fig. 8.

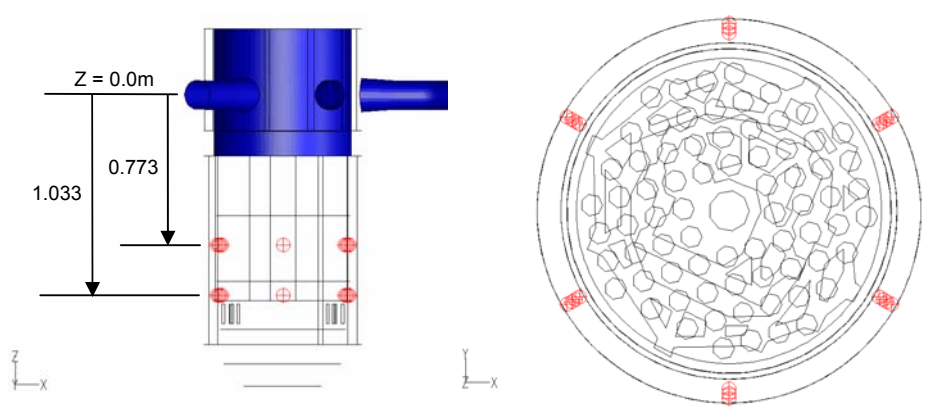


Fig. 8: Vertical levels for velocity measurements

Measured and calculated radially averaged vertical velocities are plotted in Fig. 9 for the lower vertical level in the downcomer. Qualitative agreement is good, and important non-symmetry in the flow field is visible. Below the inlet duct, however, the proportional difference is large. This could be caused by the code's inability to model the wakes adequately behind the two Hot-Leg ducts passing through the downcomer close to the inlet duct (positioned at -50° and $+70^\circ$ azimuthally from it), as they fluctuate in time, and it is impossible to represent this correctly with a steady-state calculation. The difference

could also be due to lack of resolution of the velocity field in the simulation of the stagnation zone resulting from the Cold Leg jet impingement on the inner downcomer wall, which was not investigated for mesh sensitivity effects and is a difficult region to correctly model.

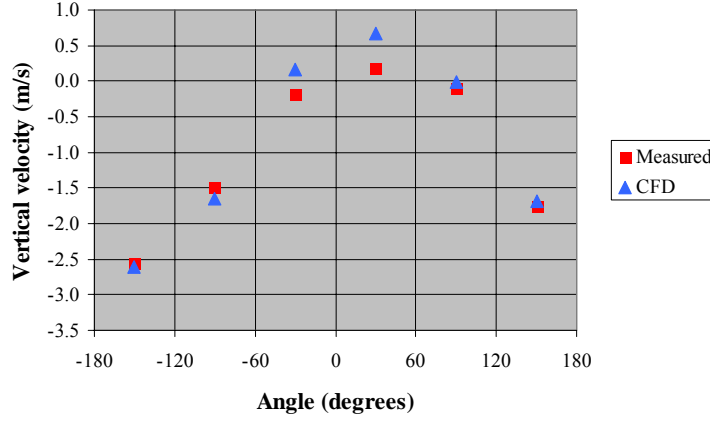


Fig. 9: Radially averaged vertical velocity at the lower level in the downcomer as a function of tangential angle (Grid 2).

Table 3 lists quantified differences between calculations and measurements for steady-state velocities, showing that deviations are higher at the middle level in the downcomer than at the lower level.

Table 3: Quantified differences between CFD calculated and measured velocities in the downcomer.

Vertical position	Velocity component	DEV3_ABS
Middle level in downcomer	Vertical	0.39
Middle level in downcomer	Tangential	0.59
Middle level in downcomer	Velocity angle	29°
Lower level in downcomer	Vertical	0.21
Lower level in downcomer	Tangential	0.32
Lower level in downcomer	Velocity angle	13°

The Absolute Deviation DEV3_ABS, is defined as:

$$DEV3_ABS = \frac{1}{n} \sum_{i=1}^n DEV2_i_ABS \quad (1)$$

where n is the number of measurement positions used for averaging, i.e. the total number of measurement positions in the core inlet plane, and DEV2 is an accumulated deviation at position i over the important time span, i.e. when the perturbation is moving through the measurement plane:

$$DEV2_i_ABS = \sum_{t=t_1}^{t=t_2} |DEV1_i|_t \quad (2)$$

and

$$DEV1_{i,t} = c_{c,i,t} - c_{m,i,t} \quad (3)$$

where c_c is the calculated, and c_m the measured, value of the velocity at position i and time t .

Vertical velocity component at the vertical elevation $Z = -1.129$ m, below the core, is plotted in Figs. 9(a) to 9(d), viewed from above, for different turbulence models but always with the High Resolution discretisation scheme (the velocity field was always more diffuse with Upwind discretisation).

The RSM model produced a slightly greater azimuthal rotation of the velocity field than the RNG model, but with reduced resolution (NB. all plots have been produced with the same velocity scale range, for clarity of comparison). Velocity distribution with the RNG model and the fine grid, Grid 2, is given in Fig. 9(d), showing that the resolution of the velocity field is significantly improved with this mesh. Discrete fluid jets emerging from the holes in the Core Support Plate are visible, and the region of upward velocity in the downcomer below the inlet duct (showing the presence of strong recirculation) shows clearer and stronger resolution across the downcomer thickness.

The conclusion was that the RNG model with High Resolution discretisation gave best agreement with measurements for steady-state conditions with the coarse mesh model, and consequently it alone was used for the fine-mesh steady-state simulation. This had also been the conclusion from earlier FLUENT calculations at Vattenfall. Scalable wall functions were the only choice with this model.

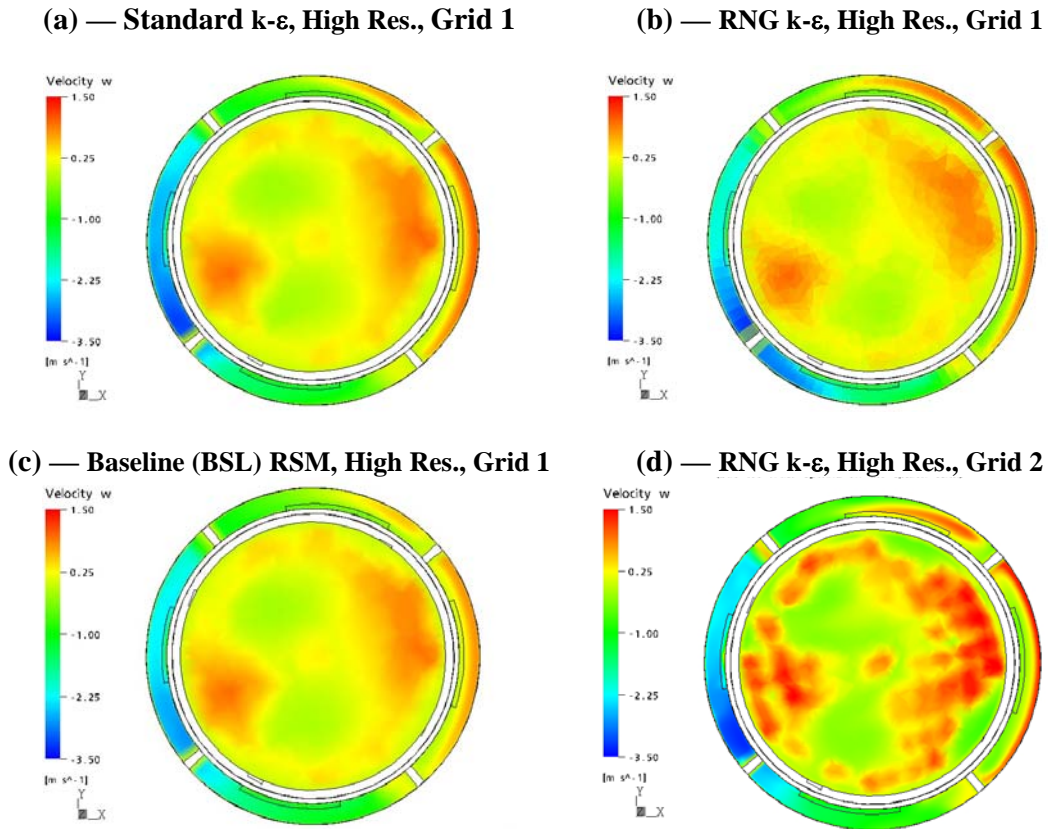


Fig. 9: Vertical velocity component at plane $Z=-1.129$ m; different grids and turbulence models

y^+ values: Grids 1 and 2

Examination on the inner downcomer wall, the hot and cold loop pipe wall, and on the inside of the lower plenum shows that the peak value of the dimensionless wall-cell distance, y^+ , for the coarse mesh steady-state simulation with RNG turbulence model and High Resolution advection scheme reached over 19000. This maximum occurred at the hot-leg penetrations, which is not expected to produce a significant error in the calculation of the flow field in the vessel as a whole. Contours of y^+ are plotted over these surfaces in Fig. 10, with a peak plotting scale range of 0 to 4500 (4500 is close to the value in the impact region of the incoming cold-leg flow on the downcomer wall).

Even with Grid 2, the peak y^+ value reached over 12000 at the hot-leg outlets. However, the values within the body of the vessel are plotted over the range 0 to 2400, giving the pattern seen in Fig. 11, with the value at the impact region of the incoming cold-leg flow close to 2400. On the basis of these y^+ values, the turbulent wall functions are being used well outside their range of applicability for the k - ϵ model (validity $30 < y^+ < 120$ in CFX-5) throughout most of the vessel, even with the fine-grid. Thus the mesh must be further refined for the wall functions to be validly applicable everywhere, and no results obtained here can be considered to be mesh-independent.

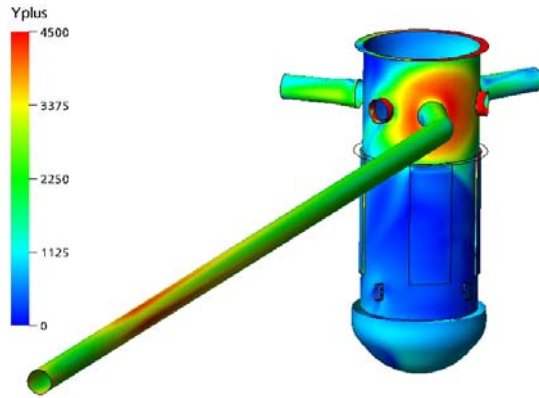


Fig. 10: y^+ contours: Grid 1

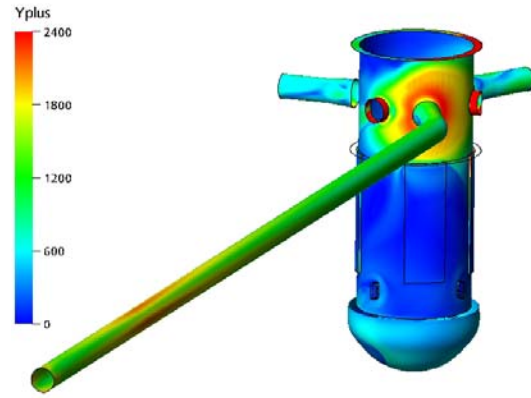


Fig. 11: y^+ contours: Grid 2

Slug-mixing transient: Grids 1 and 2

Mean and minimum dimensionless boron concentration at the core inlet as a function of time, with Grid 2, the RNG model and High Resolution discretisation, are shown in Figs. 12 and 13. The CFD calculation gives approximately the same minimum value, around 0.8, as the experiments. The calculated mean and minimum concentrations are, however, delayed by around 0.9 s compared to the measured values. This is thought to be due to inaccuracy in the measurement of flow-rate. The mass flow signal was filtered in time in the flow-meter, at a level which could not be reduced further. This resulted in a time delay in the output signal of about 0.7 s for the first indication of the slug reaching the core inlet, compared with the CFD calculations.

Figure 14 shows measured and calculated minimum boron concentrations, independent of time, at the core inlet. The inlet pipe is positioned to the right and the view is from above. It can be seen that the calculated minimum is separated from the measured minimum by about 180 mm, at the model scale of 1:5 (or around 0.52 R, where R is the radius of the core inlet plane). The displacement of the concentration field is, however, mainly azimuthal. The difference in radial position is only about 0.15 R. This could be relevant in reality, as a core is primarily different radially, as far as fuel enrichment and core reactivity are concerned.

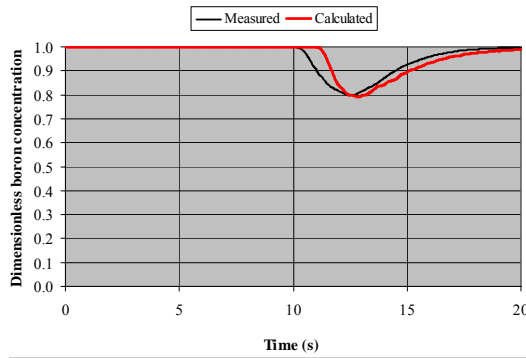


Fig. 12: Mean dimensionless boron concentration at core inlet as a function of time

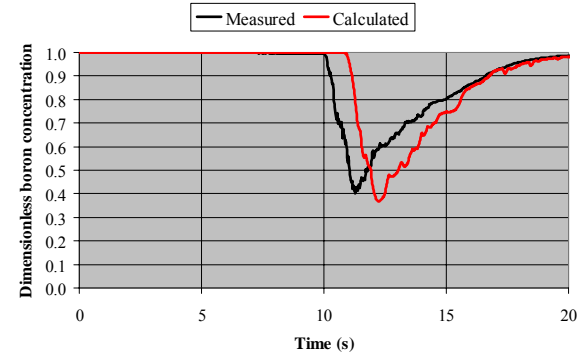


Fig. 13: Minimum relative boron concentration at core inlet (independent of position) as a function of time

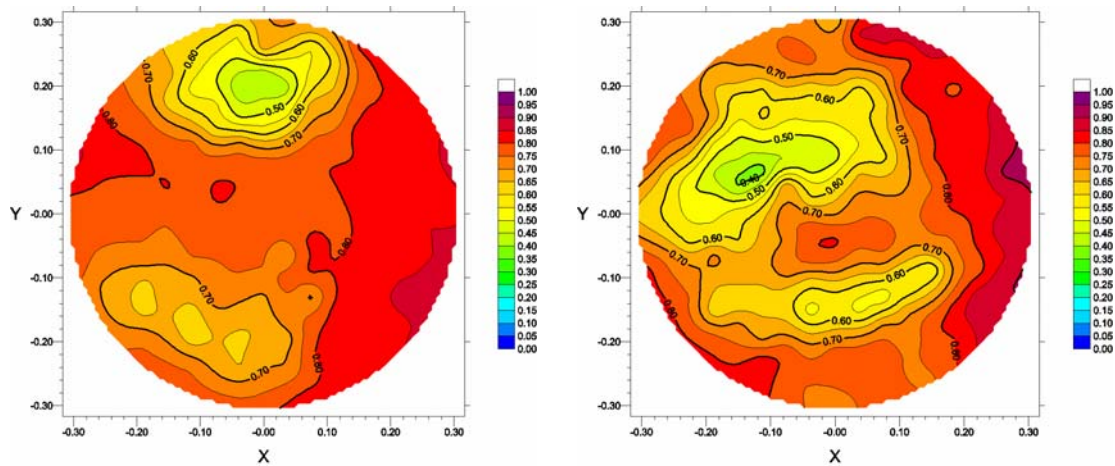


Fig. 14: Time-independent minimum relative boron concentration: Measurement left; CFD right

Two “islands” of low boron concentration are present in the measurement and the CFD calculation, and the calculated minimum concentration field shows more variations in space than that measured. The plot from the measurement is based on data for the average of five tests. Also, it should be pointed out that this is a result from a calculation that has not been verified to be grid or time-step independent.

The absolute deviation from experimental values of dimensionless boron concentration (DEV3_ABS) is 0.1228. A time shift of 0.9 s of the calculated values has been applied as well as a space shift of 176 mm, corresponding to the deviation in calculated position of the minimum concentration. Comparisons are only made over the time span when the lowest concentrations are measured, from 11.0 s to 12.0 s. Comparisons are only made around the position where the minimum concentrations were measured, over an area of 0.00915 m² (i.e. 2.8 % of the whole core inlet). This area encompasses the area for 7 probe positions, corresponding to a radius of 54 mm. Only 6 of the 7 probes were used in the comparison, as one of them was out of order during the measurements.

One reason for calculating incorrect boron concentrations at the core inlet can be that the calculated velocity field is wrong. Figures 15 to 18 show measured and calculated radially averaged vertical velocities as a function of time at the middle and lower measurement levels in the downcomer, respectively. The measured velocities shown here are averaged over a time span of about one second. Most of the fluctuations in the measured signals are therefore not visible.

It can be seen from these Figures that the rather abrupt change in flow direction at around 7 s to 10 s in the measurement at the lower level in the downcomer, and the following transition to a fully turbulent steady-state flow pattern, are not captured quite accurately by the CFD calculation. This will have an effect on the mixing and transport of the boron concentration field.

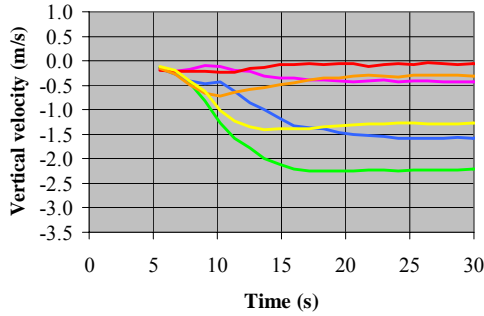


Fig. 15: Measured radially averaged vertical velocity at the middle level in the downcomer

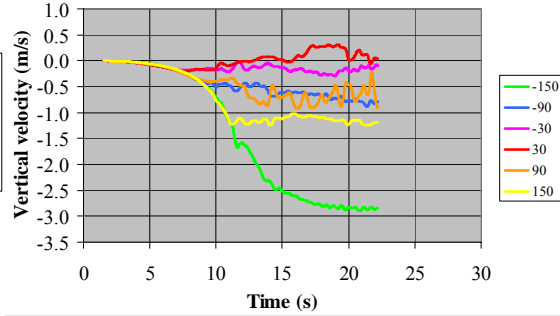


Fig. 16: Calculated radially averaged vertical velocity at the middle level in the downcomer

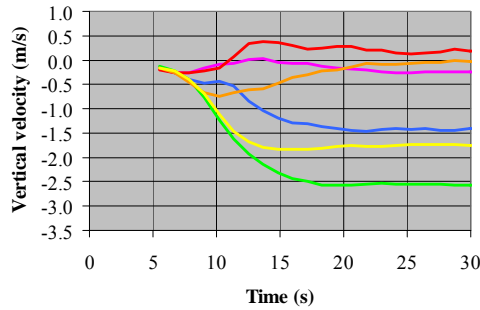


Fig. 17: Measured radially averaged vertical velocity at the lower level in the downcomer

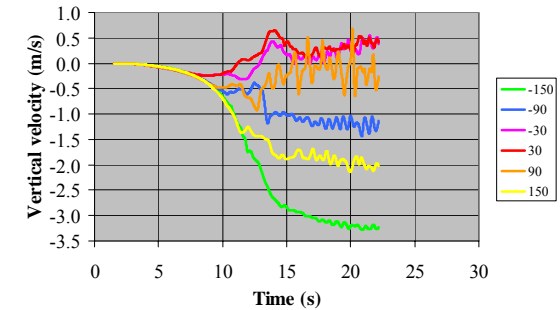


Fig. 18: Calculated radially averaged vertical velocity at the lower level in the downcomer

Flow distribution within the vessel is strongly influenced by the velocity profile at the exit of the inlet pipe. If this is incorrectly calculated, its effect will continue throughout the vessel. Shaded contours of horizontal velocity at the vertical plane where the inlet pipe joins the downcomer are plotted in Figs. 19(a) to 19(d), showing differences resulting from CFD grid coarseness and turbulence model.

The view in these figures is in the direction of flow, so the bend, which is about 3 hydraulic diameters upstream of this point, has caused the region of very low fluid velocity on the left-hand side of the inlet plane, with the RNG model and Grid 2. There is little visible difference between the profiles with the SST and RSM models, and only a small distortion of the velocity profile on the left-hand side. Isosurfaces at the front and back ends of the de-borated slug (not reproduced here) also confirmed that the RNG velocity profile is more strongly peaked and distorted than with the other turbulence models.

Further grid studies: Modelling

The High Resolution discretisation scheme was used for all calculations with Grids A to D, using the Standard $k-\epsilon$ and RNG $k-\epsilon$ turbulence models. A normalised RMS residual criterion of 10^{-5} was set for steady-state convergence, while this was relaxed to 10^{-4} for transients (the default value in all versions of CFX-5, and still recommended in CFX-10). Time-step sensitivity was examined with Grid A, using steps of 0.01 s and 0.017 s.

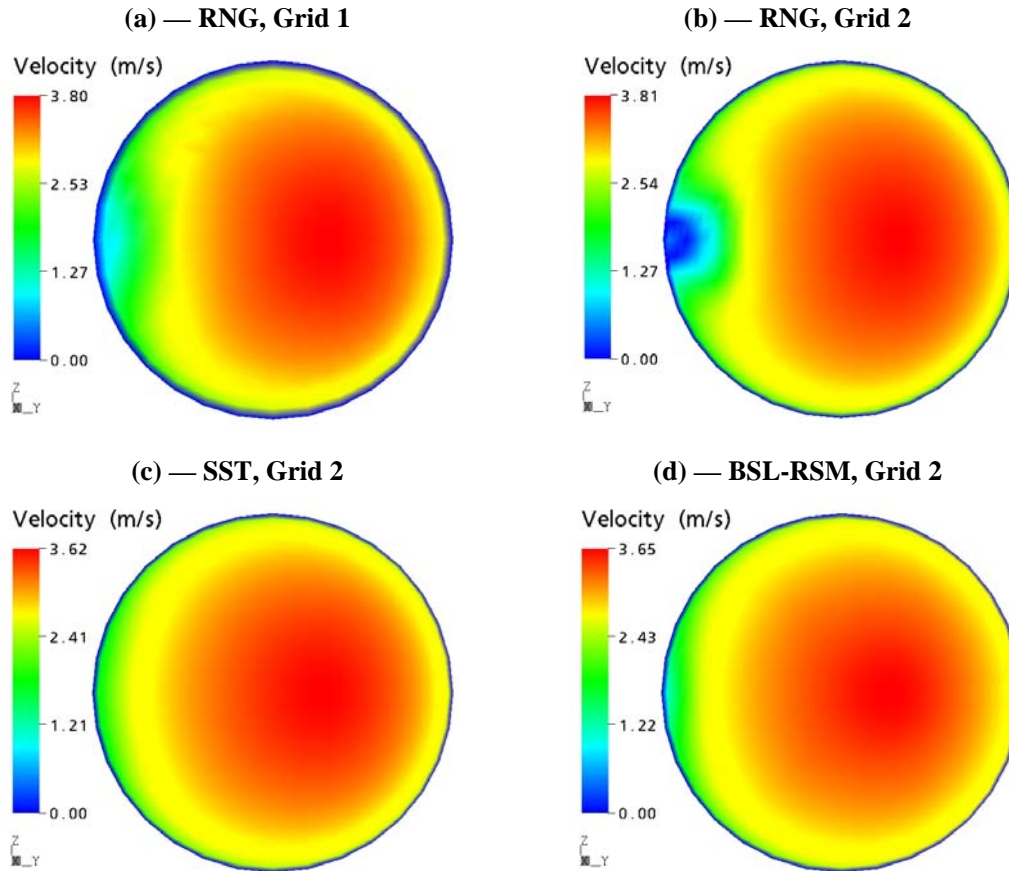


Fig. 19: Horizontal velocity component at vertical inlet plane of Cold Leg to Downcomer at 10 s

Further grid studies: Steady-state

The effects of the centring blocks and shape of the inlet pipe can be seen in Fig. 20(a) to 27(e). From Figs. 20(c) (Grid A) and 20(e) (Grid D), it can be observed that the swirl of the flow generated by the bend in the inlet pipe changes the shape and location of the vortex in the vessel. Indeed, in the solution obtained with Grid A, the region of the upward vertical velocity in the downcomer is displaced in the counter-clockwise direction compared with the solution obtained with Grid D. However, the swirl seems to have no noticeable effect on the flow at the core inlet. On the other hand, comparing Figs. 20(a) and 20(b), and Figs. 20(c) and 20(d), it can be seen that the result of introducing the centring blocks into the model of the vessel is similar to that of changing the shape of the inlet pipe: the position of the vortex in the downcomer is altered, but the flow distribution at the core inlet stays practically unaffected.

These results imply that, despite the fact that the flow velocity at the core inlet is not affected by the shape of the inlet pipe and the presence of the centring blocks, these objects change the flow in the downcomer significantly, and this suggests that they must be included in the model of the vessel for transient simulations, where the distribution of the flow velocity in the downcomer strongly affects the transport of the slug of de-borated water throughout the complete vessel. Comparing radially averaged vertical downcomer velocity with Grid A in Figs. 21 and 22, the k - ϵ model results are closer to the data at the lower measurement level, while the RNG model is closer at the middle level.

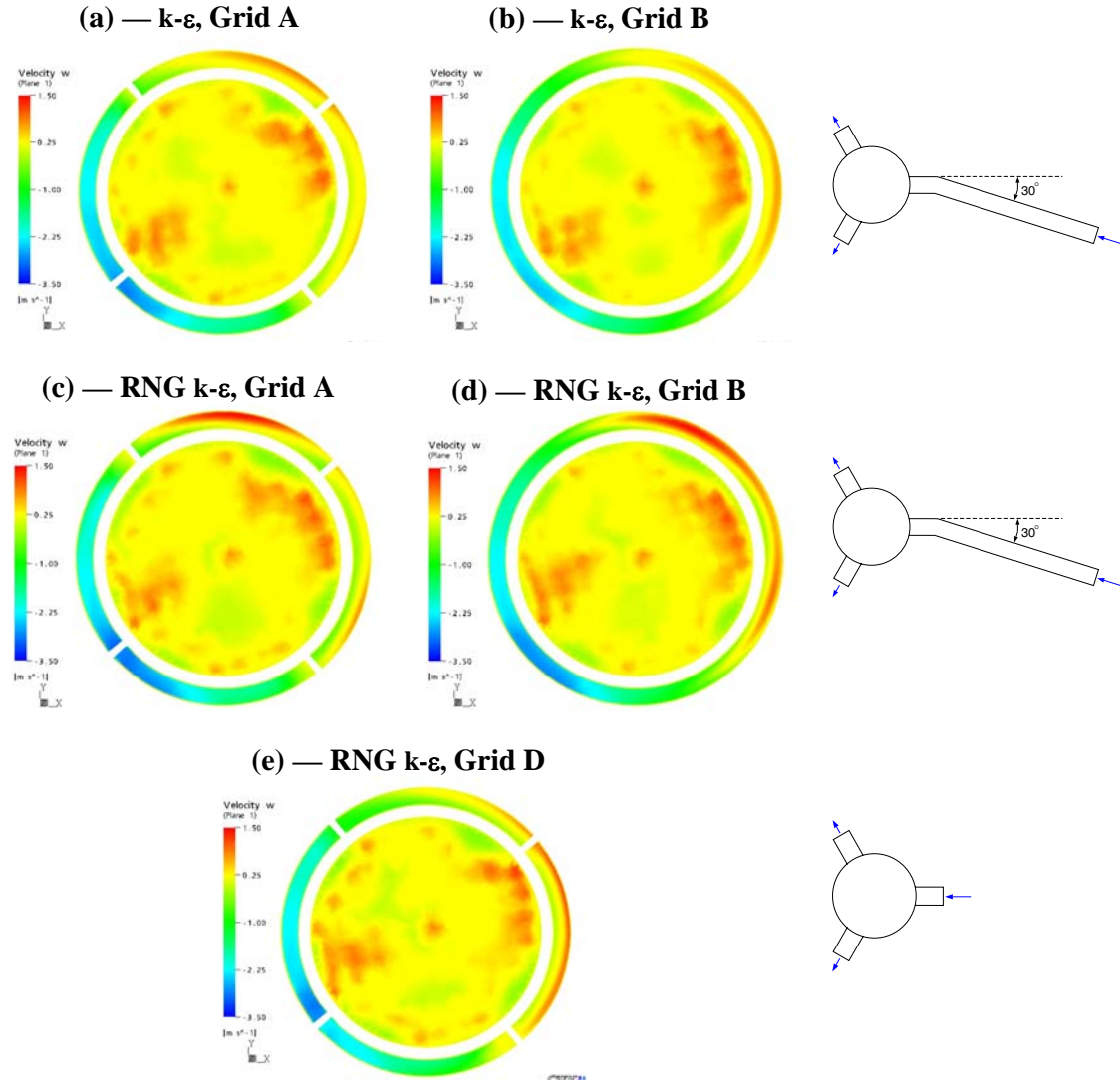


Fig. 20: Effects of the centring blocks and shape of the inlet pipe on the flow

Further grid studies: Transient

On the basis of comparison of the resolution of steady-state velocity field presented in Figs. 20(a) and 20(c), the RNG model was chosen for the transient simulations, with Grids A, B and C only. There was no significant difference between predicted transient results using time-steps of 0.01 s and 0.017 s, with Grid A and both turbulence models, so the larger value (i.e. the actual experimental data acquisition rate) was chosen for all following simulations, to minimize computational time.

The closest agreement with experiment for mean and minimum boron distribution at the Core Inlet was obtained with the RNG model, High Resolution discretisation and Grid A, as shown in Figs. 23 and 24. It can be seen in Figs. 32 and 33 that modelling of the thickness of the supporting plates in the lower plenum (Grid A) gives slightly closer agreement of mean boron concentration at Core Inlet than with zero thickness and only form-loss coefficients. For minimum concentration, the difference is even smaller.

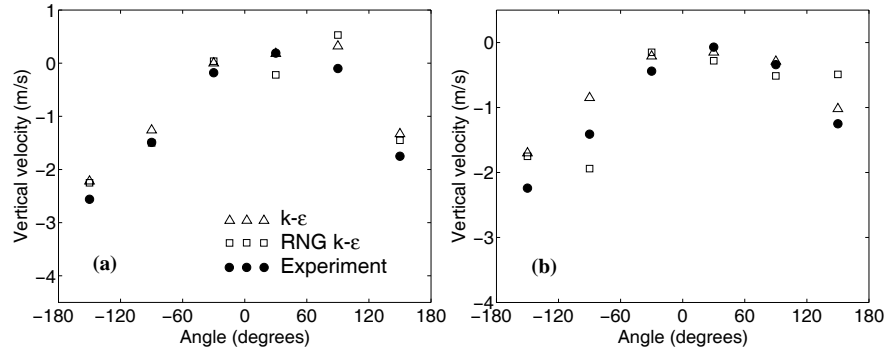


Fig. 21: Radially averaged steady-state vertical velocity in the downcomer:
(a) Lower level, $Z = -1.0033$ m; **(b)** Middle level, $Z = -0.773$ m

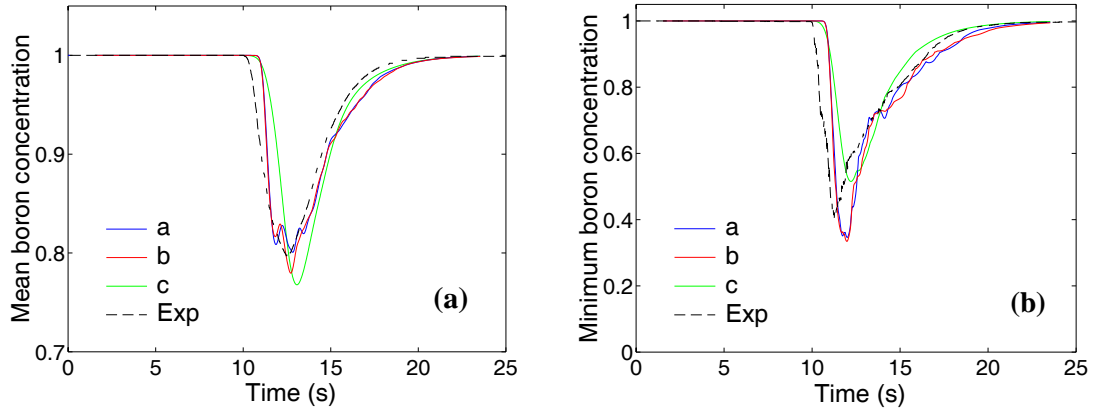


Fig. 22: Boron concentration at core inlet, RNG: **(a)** Mean; **(b)** Minimum
 Line a = Grid A, High Resolution
 Line b = Grid B, High Resolution
 Line c = Grid A, Upwind

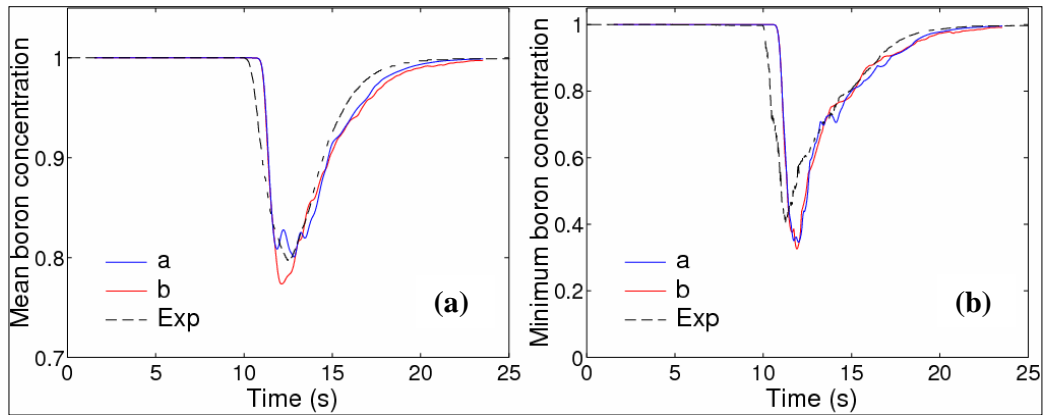


Fig. 23: Boron concentration at core inlet, RNG: **(a)** Mean; **(b)** Minimum
 Line a = Grid A, High Resolution
 Line b = Grid C, High Resolution

For the overall distribution of boron concentration at the Core Inlet at the time when the minimum occurs, it can be seen in Fig. 24 that the RNG model with Grid A agrees more closely with measurement (Fig. 25) than Grid 2 does (Fig. 26), as far as degree of rotation about the vessel axis is concerned. The magnitude of the minimum is very similar in all three plots, and in the same quadrant. However, the physical separation of the minima in the two “islands” of low concentration is smaller for both CFD simulations than was measured.

With Grid A, the weaker region of low concentration reaches a lower level than measured and is of greater extent, thus showing that the splitting and mixing of incoming flow is still not quite correct. Nevertheless, results with this grid demonstrated that it is possible to obtain very close overall and absolute agreement for minimum concentration value at the Core Inlet Plane with a grid which is only a quarter of the size of Grid 2, the finest used earlier.

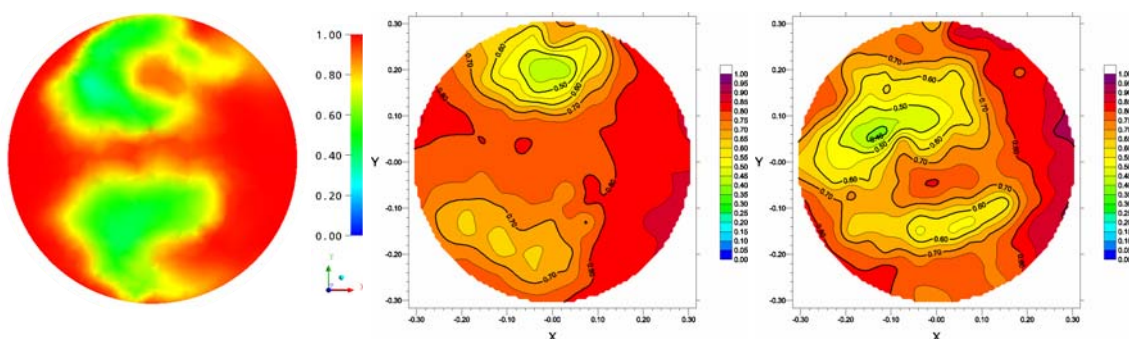


Fig. 24: Boron concentration at Core Inlet Plane: Grid A, RNG

Fig. 25: Boron concentration at Core Inlet Plane: Experiment

Fig. 26: Boron concentration at Core Inlet Plane: Grid 2, RNG

Conclusions

1. CFD calculations have been carried out on the experiment VATT-02, in the context of the FLOMIX-R EU 5th Framework Programme, to assess the capability of the CFX-5 and FLUENT codes in simulating boron dilution transients in a PWR Reactor Pressure Vessel.
2. Steady-state, isothermal simulation was made initially with two grids, an initial coarse mesh and one refined by a factor of 2 in all three dimensions. The RNG turbulence model gave results which were the nearest to measured velocities in the downcomer, with both meshes and for both codes. The reason why the RNG model is better than more sophisticated models, which can better resolve complex features of flows, is most likely because none of the models is being used with the correct range of wall-cell thickness, and the feature of the RNG model to compute lower production of turbulent kinetic energy for flow over obstacles may deal more accurately with the situation with this vessel geometry.
3. CFX-5 results were closer to measurement, with both grids, than those obtained at the initial analysis stage with FLUENT.
4. For a pump start-up transient in which a slug of de-borated water in the only operating cold leg was injected at an increasing rate, the SST model gave a minimum boron concentration over the core inlet which was about 25% above that measured. The RSM model was 25% lower than the data, while the RNG model and the fine mesh gave closest agreement with the minimum measured. However, mesh-independence of any of the results was not proven.

5. With a new set of grids, having 27% of the number of cells in the fine-mesh model previously used, it was shown that: a) it is essential to model any bends in the inlet ducting; b) mixing is improved if the thickness of the supporting plates in the lower plenum is modelled; c) rotation of flow around the vessel axis is in better agreement with experiment when the thermal shields in the downcomer are not included, suggesting that modelling of structures in the downcomer is still not correct.
6. Further simulation is needed to demonstrate the importance of including the thermal shields, their chamfered edges, and the support columns in the lower plenum. Also, the work should be continued, as more powerful computer systems become available, to refine the mesh further until mesh-independent results have been obtained.
7. Overall, it can be concluded that the present CFD study has shown closer agreement of boron concentration prediction at the core inlet than had been achieved in earlier work, with other experiments. However, care is needed in the modelling of individual components of a reactor vessel and its associated ducting in order to accurately capture the features which influence the mixing and control the flow directions, for the particular turbulence model used.

References

- 1) Rohde U., Kliem S., Höhne T., Hemström B., Toppila T., Elter J. and Bezrukov Yu., “The EC Project FLOMIX-R – Investigation of Fluid Mixing and Flow Distribution in the Reactor Circuit”, Annual Meeting on Nuclear Technology 2005, Session: Application of CFD Methods in Nuclear Reactor Safety, Nuremberg, Germany, 10–12 May 2005.
- 2) Tuomisto H., *Final Report: EUBORA Concerted Action on Boron Dilution Experiments*, EU 4th Framework Programme on Nuclear Fission Safety, AMM-EUBORA(99)-P002, Dec. 1999.
- 3) FLUENT Inc., <http://www.fluent.com/>.
- 4) CFX-5 (recently re-named ANSYS CFX-10), ANSYS Inc., Canonsburg, Pennsylvania, USA. <http://www.ansys.com/>.
- 5) Rhode U., Kleim S., Hemström B., Toppila T. and Bezrukov Y., “Description of the slug mixing and buoyancy related experiments at the different test facilities (Final report on WP 2)”, EU 5th Framework Programme 1998-2002, FLOMIX-R Deliverable D09, FIKS-CT-2001-00197, 2005.
- 6) Casey M. and Wintergerste T., *Best Practice Guidelines*, ERCOFTAC Special Interest Group on Quality and Trust in Industrial CFD, 2000.
- 7) VDI-Wärmeatlas. VDI-Verlag GmbH, Düsseldorf, 1977.
- 8) Idelchik I.E., *Handbook of Hydraulic Resistance*, 3rd Edition, Begell House Inc., 1996. ISBN Nr: 1-56700-074-6.